Current Optics and Photonics
Vol. 4, No. 5, October 2020, pp. 428-433

ISSN: 2508-7266(Print) / ISSN: 2508-7274(Online)
DOI: https://doi.org/10.3807/COPP.2020.4.5.428

Single-pixel Autofocus with Plasmonic Nanostructures

Godeun Seok[1], Seunghwan Choi[2], and Yunkyung Kim[1]*

[1]*Department of Electronics Engineering, Dong-A University, Busan 49313, Korea*
[2]*SE/Solution Business Unit, LUENSOFT INC., Seoul 05855, Korea*

(Received July 21, 2020 : revised August 29, 2020 : accepted September 9, 2020)

Recently, the on-chip autofocus (AF) function has become essential to the CMOS image sensor. An auto-focus usually operates using phase detection of the photocurrent difference from a pair of AF pixels that have focused or defocused. However, the phase-detection method requires a pair of AF pixels for comparison of readout. Therefore, the pixel variation may reduce AF performance. In this paper, we propose a color-selective AF pixel with a plasmonic nanostructure in a 0.9 μm^2 pixel. The suggested AF pixel requires one pixel for AF function. The plasmonic nanostructure uses metal-insulator-metal (MIM) stack arrays instead of a color filter (CF). The color filters are formed at the subwavelength, and they transmit the specific wavelength of light according to the stack period and incident angles. For the optical analysis of the pixel, a finite-difference time-domain (FDTD) simulation was conducted. The analysis showed that the MIM stack arrays in the pixels perform as an AF pixel. As the primary metric of AF performance, the resulting AF contrasts are 1.8 for the red pixels, 1.6 for green, and 1.5 blue. Based on the simulation results, we confirmed the autofocusing performance of the MIM stack arrays.

Keywords : Autofocus, CMOS image sensor, FDTD simulation, MIM
OCIS codes : (130.6010) Sensors; (240.6680) Surface plasmons; (130.7408) Wavelength filtering devices; (260.5950) Self-focusing

I. INTRODUCTION

With the development of the mobile phone camera, on-chip autofocus (AF) has become one of the vital functions in the CMOS image sensor. Recently, the phase detection auto focus (PDAF) method at the image plane has been used for the high-speed AF function [1-3]. The PDAF method creates a focusing function using a pair of pixels to detect the phase difference. The most widely used PDAF methods are the 1PD (one photodiode) - PDAF type, which uses a pair of exclusive pixels half-shielded by a thin metal film, and a 2PD (or Quad) - PDAF type, which uses two or four photodiodes in one pixel [1-6]. However, because half of 1PD - PDAF pixels are shielded, the amount of absorbed light is significantly reduced because the pixel size becomes smaller than 1.0 μm^2, and the metal shield generates crosstalk by reflecting the incident light [7]. In the 2PD (or Quad) - PDAF method, the photocurrent decreases while the crosstalk increases, worsening the aspect ratio as the pixel size shrinks. Consequently, due to the small pixel size, the AF performance deteriorates.

On the other hand, the surface plasmons of the nano-structures have attracted considerable interest for photonic applications. Surface plasmons are the quanta of surface-charge-density oscillations in the electron density at the surface of a metal. The surface charge oscillations are naturally coupled to electromagnetic waves [8]. By using plasmonic nanostructures such as nano-holes or nano-slit arrays, efficient conversion between photons and plasmons can be controlled at the subwavelength scale. This control provides new solutions for traditional optical processes such as color filtering and spectral imaging [9-14]. Studies of nanostructures replacing the color filter (CF) have used the metal-insulator-metal (MIM) structure [9], a hole array [10-11], and a grating structure [12-14]. The MIM structure and a hole array (array of holes) are considered to be

*Corresponding author: yunkkim@dau.ac.kr, ORCID 0000-0002-4338-7642
Color versions of one or more of the figures in this paper are available online.

capable CF for transmitting a specific wavelength [9-12]. The period of the MIM stacks is adapted for the transmission characteristics of the CF [9]. The hole array transmits a specific wavelength according to the size and arrangement of the holes [10-12]. From Satoh's researches, the surface plasmon (SP) antenna containing nano-sized metal gratings was introduced to detect light and as a refractive index [13, 14]. The SP antenna is constructed with a metal structure that converts the incident light to the optical near-field around the antenna [13]. Therefore, the SP antenna transmits the light at different wavelengths according to the period of the metal gratings and the angle of the incident light [14]. Based on these results, when the light enters at a normal angle, the peak wavelength of the transmitted light is determined by the period and width of the metal gratings. Further, when the light enters at an oblique angle, the peak wavelength of the transmitted light changes to double-humped. As a result, the transmitted light can be modulated by the metal gratings and the angle of the incident light.

In this study, we propose a novel AF pixel structure of 0.9 μm^2. A surface plasmon-based nanostructure formed by a metal (Al)-insulator (ZnSe)-metal (Al) stack array is inserted instead of the CF and functions for the AF and CF. Through an optical simulation using the finite-difference time-domain (FDTD) method, the suggested MIM structure is investigated and optimized for AF performance. Section 2 describes the concept of the AF pixel with MIM structures, and Section 3 presents and discusses the simulation results. Conclusions are presented in Section 4.

II. CONCEPT OF THE AF PIXEL WITH MIM STRUCTURES

In our study, the MIM structure is used for the 1PD-AF pixel, as shown in Fig. 1(a). The MIM structure is well known for its color recognition that can replace the CF in a conventional CMOS image sensor [9].

The MIM structure transmits the light at a specific wavelength based on the period of the MIM stack. Also, the SP antenna's metal gratings transmit the light using the period and width of gratings. Moreover, when the light enters at an oblique angle, the peak of the transmitted light is separated at both sides and the normal incidence [14]. Figure 1(a) shows the MIM structure, which transmits a specific wavelength according to the stack period, α, and the angle of the incident light, θ. Figure 1(b) shows the concept of the transmission characteristics when the light enters the MIM structure at angles from 0° to 20°. The peak transmitted light intensity at 0° appears in the wavelength λ_0. The peak wavelengths are separated by λ_{10}^{+} and λ_{10}^{-} when the angle of incident light is 10°. The separated wavelengths, λ_{θ}^{+} and λ_{θ}^{-}, can be calculated with Eq. (1) [14]. The "p" and "n" indicate a period and a

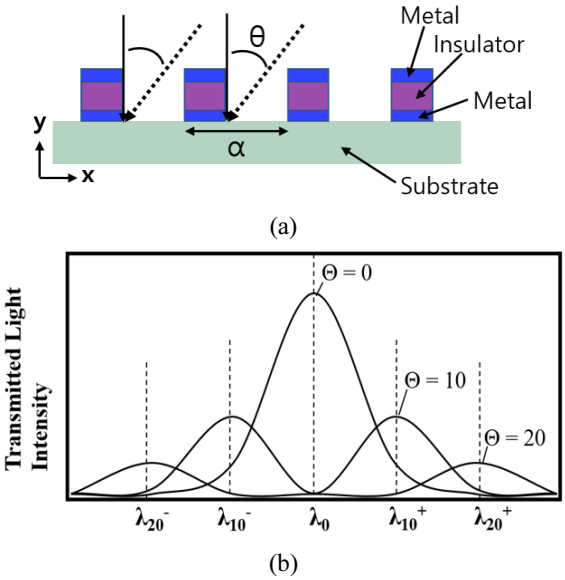

FIG. 1. Concept for the plasmonic PDAF structure. (a) Schematic diagram of the MIM nanostructure with α as the period of the gratings, and θ as the angle of the incident light. (b) Concept of the transmitted light intensity based on the wavelength and angle of the incident light. λ indicates the peak wavelength.

refractive index. The symbols Θ and λ represent the incident angle and peak wavelength. Based on these angular characteristics, we propose a new AF pixel with the MIM structure.

$$\lambda_{\theta}^{\pm} = 1/\left\{\left(\frac{1}{p}\right) \pm \left(\frac{n}{\lambda}\right)\sin\theta\right\}. \quad (1)$$

Figure 2 is a flowchart that shows the path from the simulated spectral characteristics to the calculation of the AF contrast as the AF performance. We can obtain the spectral features from the optical simulation when the wavelength is from 400 nm to 700 nm. Light of this range is incident on the suggested pixel at the incident angles from 0° to 20°. As shown in Fig. 2(a), the spectral characteristics indicate the relation between the absorbed photon density and the wavelength. To obtain the angular response, the absorbed photon density is integrated from 400 nm to 700 nm at each incident angle. The integrated results are shown in Fig. 2(b). Although light of this range is simulated at the incident angles from 0° to 20°, the absorbed photon density is the same from 0° to -20°. Because the MIM structure is symmetric. Therefore, the angular response can be drawn by inversion, as shown in Fig. 2(c). We can evaluate the AF performance and the AF contrast in Figs. 2(d), 2(e). The peak sensitivity at 0° indicates the focusing status. The other angle is the defocusing status. As shown in Fig. 2(e), the AF contrast is obtained by dividing the peak sensitivity by crosstalk at the incident angles from -20° to 20°.

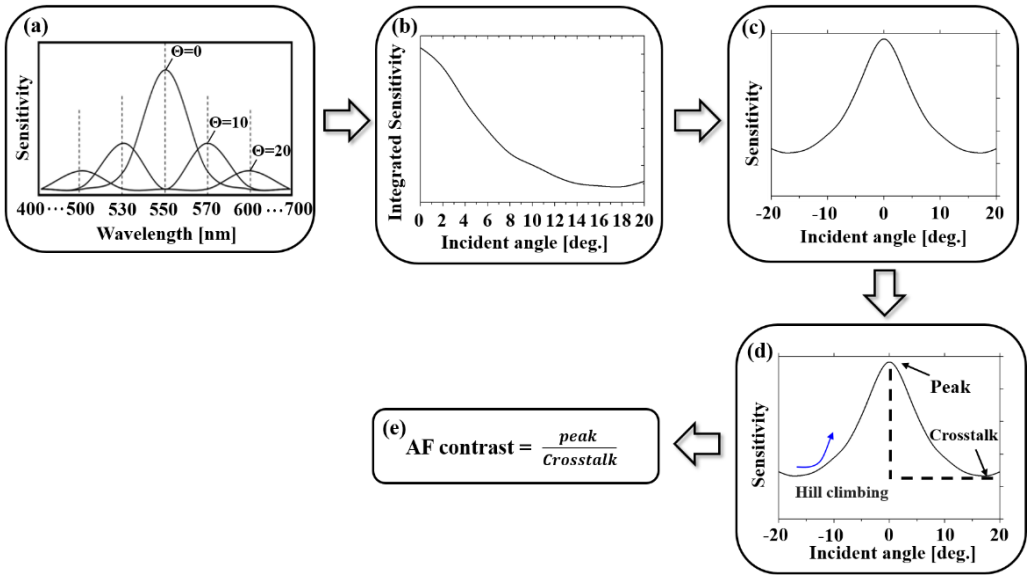

FIG. 2. Flowchart for AF function from the simulation results.

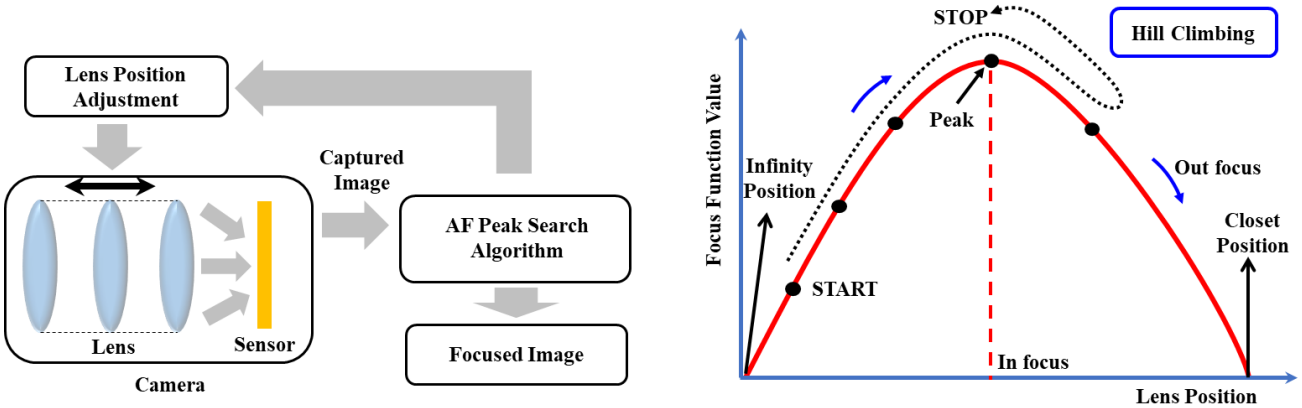

FIG. 3. (a) The concept diagram of the CDAF method. (b) Hill Climbing algorithm used to find the optimal lens position in the CDAF method.

The question arises: how can we define the AF performance based on the simulation results? What is the basis for the AF contrast calculation? Figure 3(a) shows the concept for the presupposed AF system based on the contrast-detection autofocus (CDAF) system. The CDAF is an auto-focusing technology that moves the lens until the focus reaches the highest contrast [15-17]. A CDAF system generally operates iteratively [15]. First, an image is captured by the camera at the current lens position. Next, the selection of the focusing region determines which part of the captured image is used to compute sharpness. Then, the sharpness measurement is applied to the focusing region to calculate the focusing value. Finally, a peak search is conducted to obtain the best lens position from the focusing value candidates. As shown in Fig. 3(b), the peak search algorithm CDAF uses the hill-climbing method, therefore requiring one pixel's angular response for the AF function [16, 17]. The in-focus position is indicated at the peak sensitivity of the angular response. The lens is then focused instantly based on the calculated focusing amount and the direction. As the critical AF performance, AF contrast is defined as the AF sensitivity ratio between the highest sensitivity and the lowest sensitivity. The AF contrast is typically used as the index for AF performance [5]. Eventually, the AF contrast can be derived using the same equation, as shown in Fig. 2(e).

III. SIMULATED RESULTS AND DISCUSSION

To analyze the suggested pixel structure, the optical characteristics were investigated using an optical simulator [18]. The AF performance was investigated using the FDTD method [3-6], and the plasmon effect of the image

sensor was established [9-14]. Figure 4(a) shows the 2D simulated pixel structure for the green pixels. The MIM array serves as a color filter located between the microlens and photodiodes. As shown in Fig. 4(b), the MIM stack has aluminum (Al)-zinc selenide (ZnSe)-aluminum (Al) layers in the SiO_2 (silicon dioxide) layers. The thickness of the Al layer is 40 nm, and ZnSe layers are 100 nm thick. In Fig. 4(b), the "p" and "w" are the MIM stack's period and width. The MIM stack array functions not only as the AF but as the CF. Therefore, the structure parameters of the red, green, and blue pixels are optimized for period, width, and thickness. The simulated pixel pitch is 0.9 μm as below 1.0 μm. The silicon photodiode is 3.0 μm thick. As shown in Fig. 4(a), a plane wave with wavelengths from 400 to 700 nm was evident in the y-axis. The boundary conditions were periodic on the X-axis and a perfect match layer (PML) on the Y-axis. The minimum mesh size was 3 nm. The radius of curvature (ROC) and the height of the microlens were optimized at 0.7 μm and 0.5 μm. The optical constants for all the materials were obtained from the literature [19, 20].

The period of MIM stack array was investigated to optimize the transmittance of the incident light for the CF and AF pixels. In this simulation, the absorption ratio of photons was calculated from the transmitted light in the photodiode. The absorption ratios at the incident angles from 0° to 20° were simulated in TE and TM mode. As shown in Fig. 5, the peak wavelengths at the incident

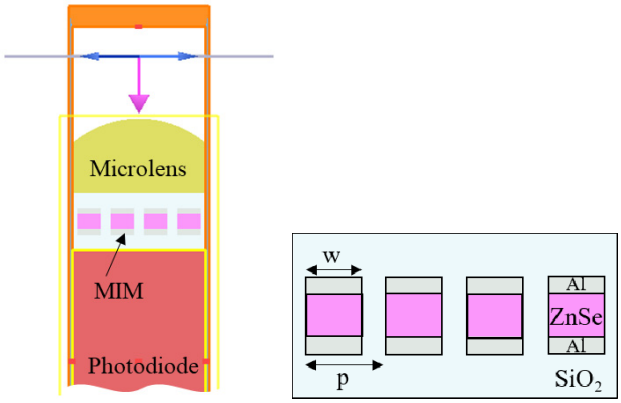

(a) (b)

FIG. 4. (a) Simulated structure of the green pixel. The pixel has different periods of MIM arrays for red, green, and blue. (b) Simulated MIM stack array with Al-ZnSe-Al. The period "p" is changed to adapt to the wavelength of the peak absorption ratio modulation. The thickness and width of each layer are shown in Table 1.

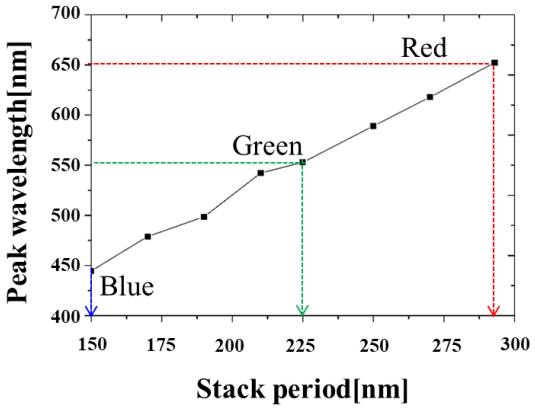

FIG. 6. Peak wavelength according to the stack period. The stack period was estimated to 293 nm for red pixels, 225 nm for green, and 150 nm for blue.

TABLE 1. Optimized parameters of the PDAF pixel

	Red pixel	Green pixel	Blue pixel
w (width)	205 nm	157.5 nm	105 nm
p (MIM stack period)	293 nm	225 nm	150 nm
Duty ratio (w/p)	0.7		
Al thickness	40 nm		
ZnSe thickness	100 nm		
SiO_2 thickness	380 nm		

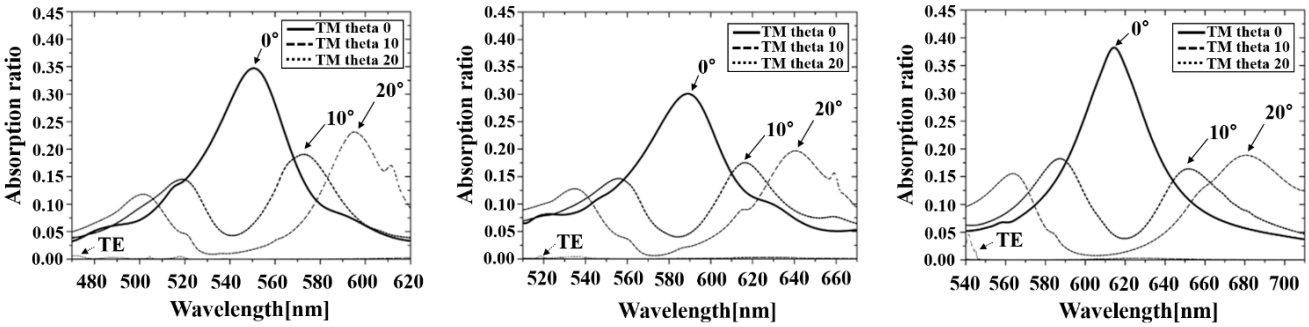

(a) (b) (c)

FIG. 5. The simulation results in the TE and TM mode when the MIM stack periods were 225 nm, 250 nm, and 270 nm. The ratio of absorption photon density according to the period, p, of the MIM stack, and incident light angle. The results show the relationship between the period and the peak wavelength. (a) p = 225 nm, (b) p = 250 nm, and (c) p = 270 nm.

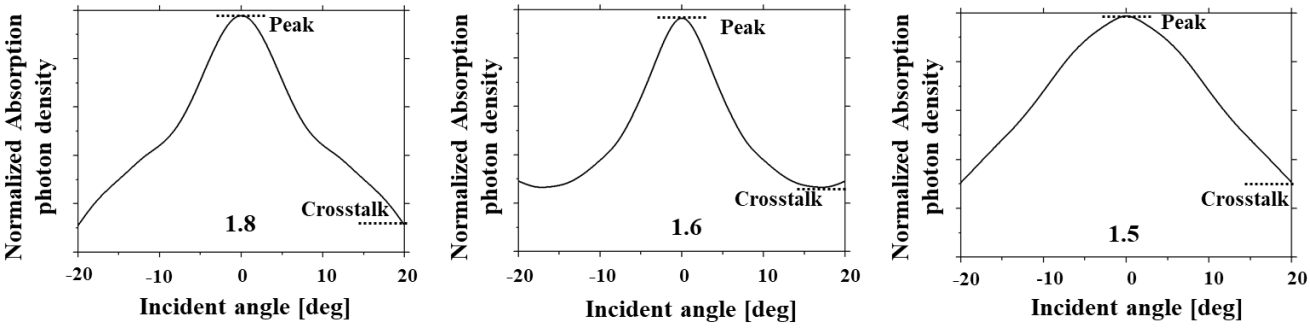

FIG. 7. Angular response of the normalized absorption photon density. The AF contrast is shown in the middle of each graph. (a) 293 nm (red pixel), (b) 225 nm (green pixel), and (c) 150 nm (blue pixel).

angle of 0°, 10°, and 20° shifted to a longer wavelength as the period increased. Also, the E-field is perpendicular to the Al grating, the absorption ratios of the TE mode are extremely low. Figure 6 shows the simulated absorption ratios based on the different MIM stack periods and the incident angles of light. As the same results in Fig. 5, the absorption ratio's peak wavelength was shifted to a shorter wavelength as the MIM stack period decreased. Finally, the periods of the MIM structure having a peak absorption ratio in the wavelengths of 650 nm (red), 550 nm (green), and 450 nm (blue) at a normal angle of incidence are determined as 293 nm, 225 nm, and 150 nm, respectively. Table 1 shows the MIM stack structure's parameter for the red, green, and blue pixels without a CF array.

As summarized in Table 1, the angular response for verification of the AF performance was derived from the simulated absorbed photon density of the red, green, and blue pixels. Using the process shown in Fig. 4, the angular response of each red, green, and blue pixel was obtained and is shown in Fig. 7. The AF contrast was calculated by dividing the highest value (peak) by the lowest value (crosstalk) of a normalized absorbed photon density. The AF contrast for each red pixel was 1.8, 1.6 for green, and 1.5 for blue. The AF performance was confirmed with the suggested MIM structure in the 0.9 μm^2 pixel.

IV. CONCLUSIONS

We introduced a new AF pixel structure with a plasmonic nanostructure in a 0.9 μm^2 pixel. Surface plasmon-based nanostructures formed by metal (Al)-insulator (ZnSe)-metal (Al) stack arrays transmitted light of a specific wavelength depending on the MIM stack period and incident angle for the CF array. The pixel having the MIM array was confirmed as the AF function using the suggested AF algorithm. Thus, the MIM array of all the pixels performed with both the CF array and the AF pixels. Using the FDTD simulation, the AF contrast was obtained as the AF performance, which was 1.8 for red pixels, 1.6 for green, and 1.5 for blue.

Based on these results, thinner and multi-functional pixels for a CMOS image sensor could be developed in an extremely small pixel pitch. Only half the thickness of the typical CF would be used for the CF function in 0.9 μm^2. The aspect ratio was enhanced by shrinking the optical path for the small pixel pitch. Moreover, the recommended pixel functioned as the AF pixel without the additional layer. We confirmed that the recommended pixel structure with a MIM array performing as the CF and AF pixels demonstrates its potential for the future pixel.

ACKNOWLEDGMENT

This paper was the product of a research project supported by SK Hynix Inc.

REFERENCES

1. S. Uchiyama, "Superiority of image plane phase detection AF," J-Stage, Japan, ITE Technical Report, **36**, Sep. 21, 2012. [Online]. Available: https://www.jstage.jst.go.jp/article/itetr/36.38/0/36.38_17/_article/-char/en
2. H. Endo, ""Phase detection pixel built-in image sensor" to realize high speed auto focus," J. Inst. Image Inf. Telev. Eng., **65**, 290-292 (2011).
3. M. Kobayashi, M. Johnson, Y. Wada, H. Tsuboi, H. Takada, K. Togo, T. Kishi, H. Takahashi, T. Ichikawa, and S. Inoue, "A low noise and high sensitivity image sensor with imaging and phase-difference detection AF in all pixels," ITE Trans. Media Technol. Appl. **4**, 123-128 (2016).
4. A. Morimitsu, I. Hirota, S. Yokogawa, I. Ohdaira, M. Matsumura, H. Takahashi, T. Yamazaki, H. Oyaizu, Y. Incesu, M. Atif, and Y. Nitta, "A 4M pixel full-PDAF CMOS image sensor with 1.58 μm 2×1 On-Chip Micro-Split-Lens technology," ITE Tech. Rep. **39**, 5-8 (2015).
5. S. Choi, K. Lee, J. Yun, S. Choi, S. Lee, J. Park, E. Shim, J. Pyo, B. Kim, M. Jung, Y. Lee, K. Son, S. Jung, T. Wang, Y. Choi, D. Min, J. Im, C. Moon, D. Lee, and D. Chang, "An all pixel PDAF CMOS image sensor with 0.64

μm × 1.28 μm photodiode separated by self-aligned in-pixel deep trench isolation for high AF performance," in *Proc. Symposium on VLSI Technology* (Kyoto, Japan, Jun. 2017), pp. T104-T105.
6. T. Okawa, S. Ooki, H. Yamajo, M. Kawada, M. Tachi, K. Goi, T. Yamasaki, H. Iwashita, M. Nakamizo, T. Ogasahara, Y. Kitano, and K. Tatani, "A 1/2 inch 48M all PDAF CMOS image sensor using 0.8 μm Quad Bayer Coding 2 × 2OCL with 1.0 lux minimum AF illuminance level," in *Proc. IEEE International Electron Devices Meeting (IEDM)* (San Francisco, CA, USA, Dec. 2019), pp. 16.3.1-16.3.4.
7. D. N. Yaung, B. C. Hsieh, C. C. Wang, J. C. Liu, T. J. Wang, W. D. Wang, C. C. Chuang, C. Chao, Y. L. Tu, C. S. Tsai, T. L. Hsu, F. Ramberg, W. P. Mo, H. Rhodes, D. Tai, V. C. Venezia, and S. G. Wuu, "High performance 300 mm backside illumination technology for continuous pixel shrinkage," in *Proc. International Electron Devices Meeting* (Washington, DC, USA, Dec. 2011), pp. 8.2.1-8.2.4.
8. L. Novotny and B. Hecht, *Principles of Nano-optics,* 2nd Ed. (Cambridge University Press, Cambridge, UK, 2012), Chapter 12.
9. T. Xu, Y.-K. Wu, X. Luo, and L. J. Guo, "Plasmonic nano-resonators for high-resolution colour filtering and spectral imaging," Nat. Commun. **1**, 59 (2010).
10. Y. Horie, S. H. Han, J. Y. Lee, J. W. Kim, Y. S. Kim, A. Arbabi, C. G. Shin, L. Shi, E. Arbabi, S. M. Kamali, H. S. Lee, S. W. Hwang, and A. Faraon, "Visible wavelength color filters using dielectric subwavelength gratings for backside-illuminated CMOS image sensor technologies," Nano Lett. **17**, 3159-3164 (2017).
11. H. J. Cho and Y. S. Do, "Plasmonic color filter with robustness against cross talk for compact imaging applications," Curr. Opt. Photon. **4**, 16-22 (2020).
12. B. Y. Zheng, Y. Wang, P. Nordlander, and N. J. Halas, "Color-selective and CMOS-compatible photodetection based on aluminum plasmonics," Adv. Mater. **26**, 6318-6323 (2014).
13. H. Satoh and H. Inokawa, "Surface plasmon antenna with gold line and space grating for enhanced visible light detection by a silicon-on-insulator metal-oxide-semiconductor photodiode," IEEE Trans. Nanotechnol. **11**, 346-351 (2012).
14. H. Satoh, T. Aso, S. Iwata, A. Ono, and H. Inokawa, "Refractive index measurement of aqueous solution using silicon-on-insulator photodiode with surface plasmon antenna," in *Proc. Asia-Pacific Workshop on Fundamentals and Applications of Advanced Semiconductor Devices* (Hakodate, Japan, Jul. 2016), pp. 70-73.
15. X. Xu, Y. Wang, J. Tang, X. Zhang, and X. Liu, "Robust automatic focus algorithm for low contrast images using a new contrast measure," Sensors **11**, 8281-8294 (2011).
16. X. Zhang, Z. Liu, M. Jiang, and M. Chang, "Fast and accurate auto-focusing algorithm based on the combination of depth from focus and improved depth from defocus," Opt. Express **22**, 31237-31247 (2014).
17. P. Śliwiński and P. Wachel, "A simple model for on-sensor phase-detection autofocusing algorithm," J. Comput. Commun. **1**, 11-17 (2013).
18. Lumerical Inc., "FDTD 3D electromagnetic simulator," (FDTD), https://www.lumerical.com/products/fdtd/ (Accessed Date: 23 September 2020).
19. H. Taguchi and M. Enokido, "Technology of color filter materials for image sensor," in *Proc. International Image Sensor Workshop* (Hokkaido, Japan, Jun. 2011), pp. 34-37.
20. D. T. F. Marple, "Refractive index of ZnSe, ZnTe, and CdTe," J. Appl. Phys. **35**, 539-542 (1964).